Supporting Information

Ru nanoparticles decorated $Ni(OH)_2$ nanosheets for highly efficient electrochemical synthesis of 2,5-furandicarboxylic acid: experimental and theoretical studies

Zhong Cheng,[a] Dingbang Fu,[a] Wenjing Zhou,[a] Wenfang Deng,*[a,b] Yueming Tan,*[a] Ming Ma*[a]

Key Laboratory of Chemical Biology and Traditional Chinese Medicine Research (Ministry of Education of China), College of Chemistry and Chemical Engineering, Hunan Normal University, Changsha 410081, China

E-mail: Dengwenfang@hunnu.edu.cn (W. Deng); tanyueming0813@hunnu.edu.cn (Y. Tan); mingma@hunnu.edu.cn (M. Ma).

Chemicals and Materials

Nickel nitrate hexahydrate ($Ni(NO_3)_2 \cdot 6H_2O$, AR), urea ($CO(NH_2)_2$, AR), ammonium fluoride (NH_4F, AR), ethylene glycol($(CH_2OH)_2$, AR) and ethanol (AR) were purchased from Sinopharm Chemical Reagent Co. Ltd. Ruthenium chloride ($RuCl_3$, AR) was purchased from Shanghai Macklin Biochemical Reagents Co. Ltd. The chemicals of 5-hydroxymethylfurfural (HMF), 2,5-furandicarboxylic acid (FDCA), 5-hydroxymethyl-2-furancarboxylic acid (HMFCA), 2,5-diformylfuran (DFF), 5-formyl-2-furancarboxylic acid (FFCA), Nafion (5wt.%) were purchased from Sigma-Aldric. Nickel foam (NF) was purchased from Sheng Qiang Co. Ltd. Distilled water (18.25 MΩ cm^{-1}) from a system (Milli-Q) was used in all experiments. All the chemicals were used without purification.

Characterization techniques

Scanning electron microscope (SEM) images were taken by a FEI SEM450. Scanning transmission electron micrographs (STEM), HAADF-STEM images and energy dispersive X-ray spectroscopy (EDS) elemental mapping were carried out on a Thermo Fisher Scientific Talos F200X S/TEM instrument with an accelerating voltage of 200 kV, respectively. X-ray diffraction (XRD) patterns were obtained with an Ultima IV powder diffractometer using Cu Kα radiation (λ = 1.5406 Å). X-ray photoelectron spectra (XPS) was detected by the Thermo ESCALAB 250Xi (Thermo Electron, U.K.) with Al Kα X-ray source. The Raman spectra were recorded at room temperature on a Thermo DXR instrument with a 780 nm excitation laser. The water contact angles were measured via an optical contact angle measuring system (TX500TM, USA KINO Industry Co. Ltd). In situ Raman spectra were characterized by the confocal Raman microscope (Horiba JY HR Evolution with 532 nm laser). All electrochemical studies were carried out on a CHI 760E electrochemical Station (Shanghai Chenhua). A HgO/Hg (1.0 M KOH)

electrode and a Pt foil (1 × 1 cm) were used as the reference and the counter electrodes, respectively. The potentials measured in this work were converted to reversible hydrogen electrode (RHE) using the Nernst equation: E (RHE) = E (HgO/Hg) + 0.098 V + 0.059 × pH. In-situ Raman spectra were characterized by the confocal Raman microscope (Renishaw's Invia Reflex microscopy). High performance liquid chromatography (HPLC, Shimadzu Prominence LC-20AT, Japan) with an ultraviolet-visible detector was used to analyze HMF, and the intermediates and products during HMF oxidation.

Theoretical calculation

All density functional theory (DFT) calculations were conducted via the Vienna ab initio simulation package (VASP). The generalized gradient approximation (GGA) functional of Perdew, Burke, and Ernzerhof (PBE) was employed for the electron exchange and correlation energy for structural relaxation. The energy cutoff for the plane wave basis expansion was set to 450 eV and the force on each atom less than 0.02 eV/Å was set for the convergence criterion of geometry relaxation. After optimization, the cuboctahedral Ru_{13} nanoparticle is distorted. The distorted cuboctahedron nanoparticle is more stable than the other symmetry configurations by calculating the formation energy. The force convergence criterion was set to -0.02 eV/Å and energy convergence criterion was 10^{-4} eV. The self-consistent calculations apply a convergence energy threshold of 10^{-4} eV. A vacuum layer of 20 Å was adopted. We employ cuboctahedral Ru_{13} nanoparticle on $Ni(OH)_2$-(001) surface by referring to previous work. The HMF adsorption energy was calculated by the following equation:

$$E_{surface\text{-}HMF} = E_{surface\text{-}HMF} - E_{surface} — E_{HMF}$$

where $E_{surface\text{-}HMF}$, $E_{surface}$ and E_{HMF} represent the total energy of the pristine surface with HMF, surface energies and the energy of HMF, respectively. The Gibbs free energy change (ΔG) of each step is

calculated using the following formula:

$$\Delta G = \Delta E + \Delta ZPE - T\Delta S$$

where ΔE is the electronic energy difference directly obtained from DFT calculations, ΔZPE is the zero point energy difference, T is the room temperature (298.15 K) and ΔS is the entropy change. ZPE could be obtained after frequency calculation.

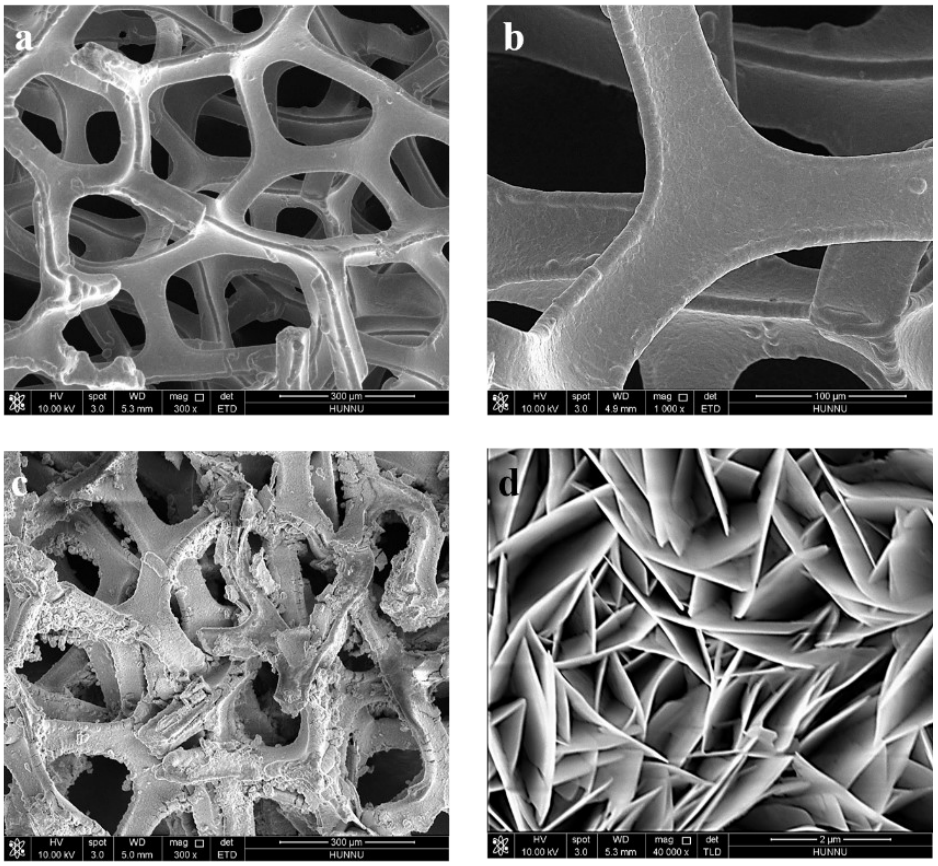

Fig. S1. SEM images of (a, b) Ni foam and (c, d) $Ni(OH)_2$/NF at different magnification.

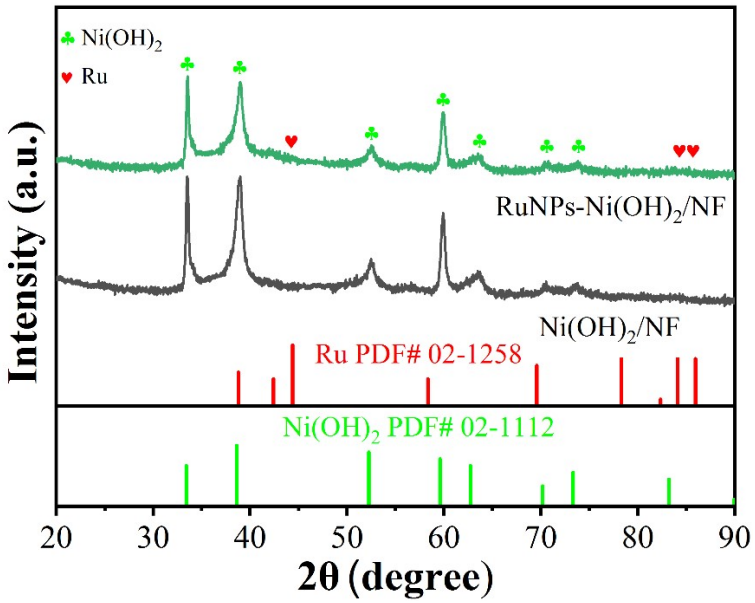

Fig. S2. XRD patterns of $Ni(OH)_2$/NF and RuNPs-$Ni(OH)_2$/NF catalysts.

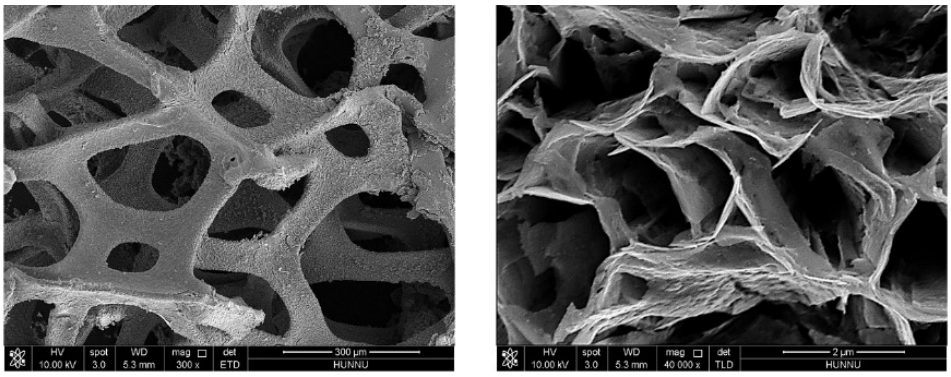

Fig. S3. SEM images of RuNPs-$Ni(OH)_2$/NF at different magnification.

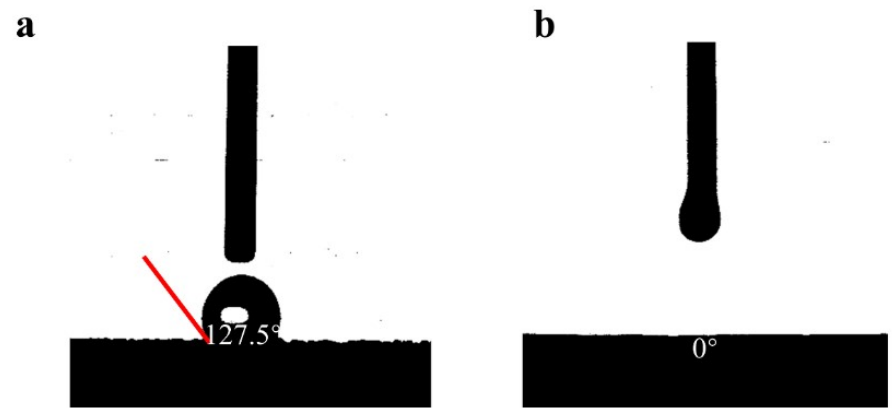

Fig. S4. Water contact angles of (a) NF and (b) RuNPs-$Ni(OH)_2$/NF.

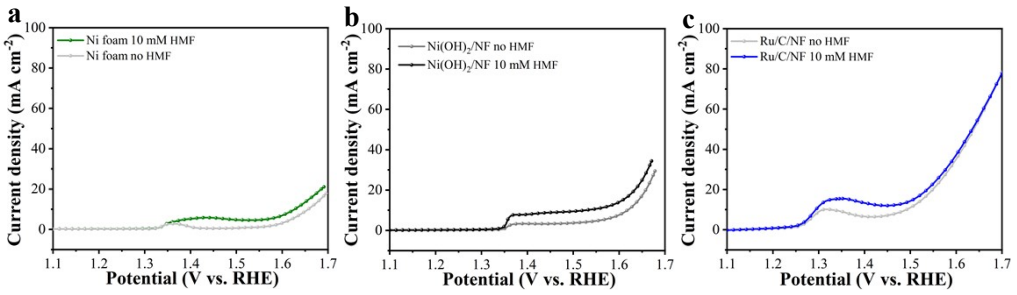

Fig. S5. LSV curves of (a) bare NF, (b) $Ni(OH)_2$/NF, and (c) Ru/C/NF in 1.0 M KOH aqueous solution with and without 10 mM HMF.

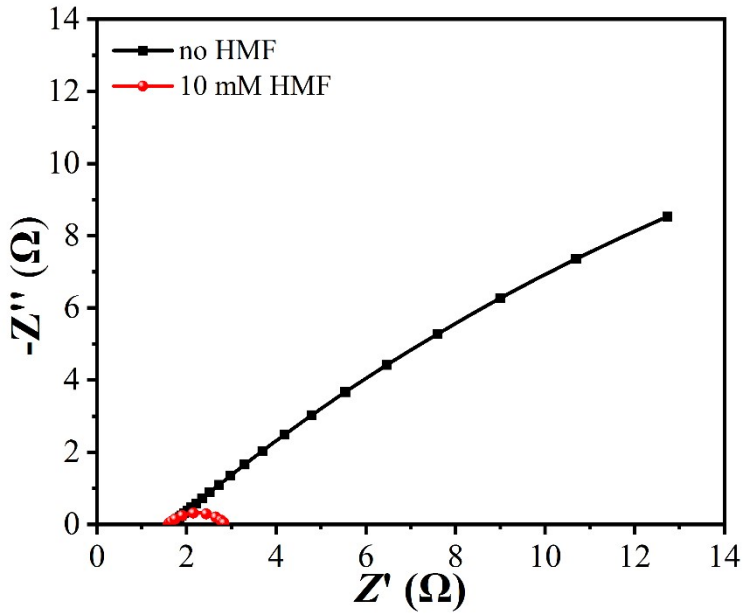

Fig. S6. Nyquist plots for RuNPs-Ni(OH)$_2$/NF in 1 M KOH with and without 10 mM HMF at 1.45 V (vs. RHE).

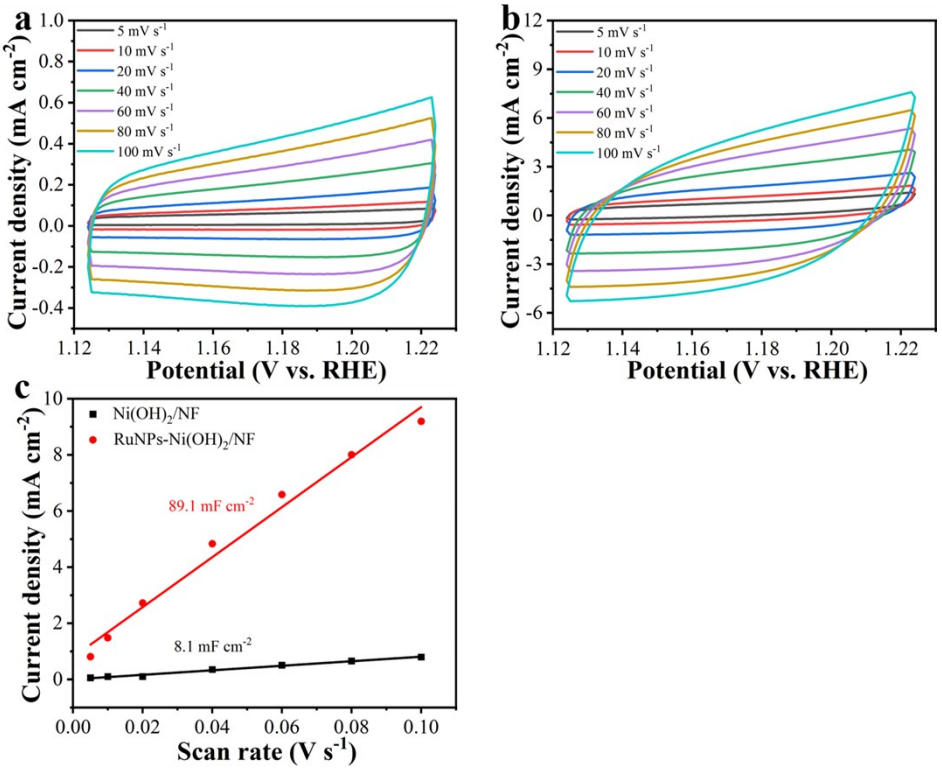

Fig. S7. CVs curves of (a) $Ni(OH)_2$/NF and (b) RuNPs-$Ni(OH)_2$/NF at various scan rates (5 to 100 mV s^{-1}). (c) The C_{dl} of $Ni(OH)_2$/NF and RuNPs-$Ni(OH)_2$/NF.

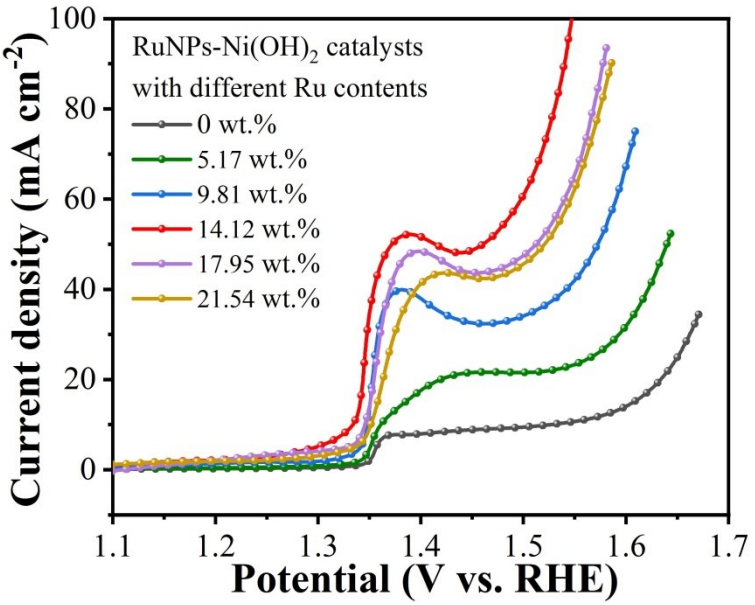

Fig. S8. LSV curves of RuNPs-$Ni(OH)_2$/NF catalysts with different Ru contents. RuNPs-$Ni(OH)_2$/NF electrodes with different Ru contents were prepared by using 0, 20, 40, 60, 80, 100 mg of $RuCl_3$ as the metal precursors, respectively.

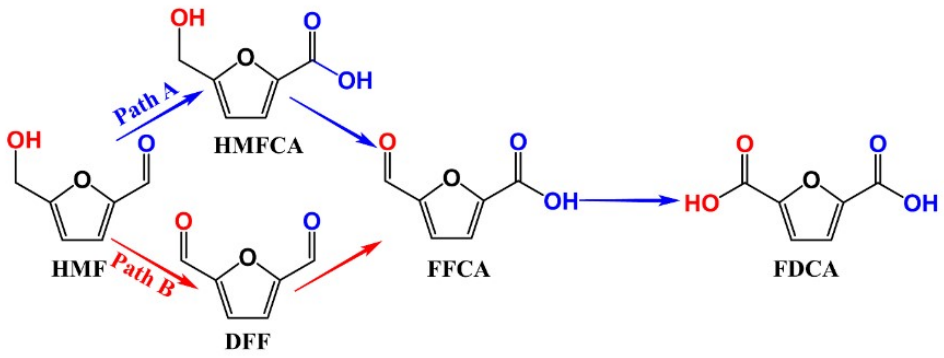

Fig. S9. Two possible pathways of HMF oxidation to FDCA.

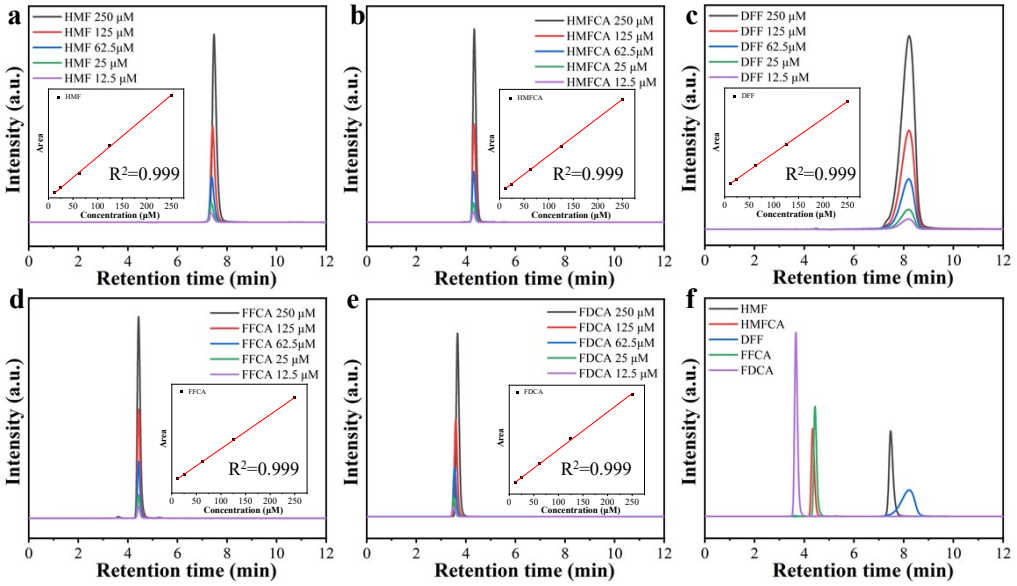

Fig. S10. (a-e) The HPLC standard curves of HMF and corresponding products. (f) The elution curve of related standard mixtures.

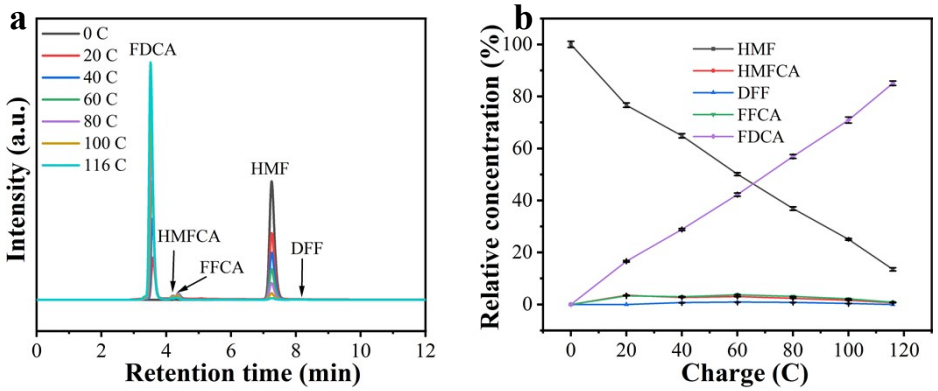

Fig. S11. (a) HPLC elution profiles and (b) concentration changes during HMFOR catalyzed by $Ni(OH)_2$/NF as functions of charge consumption.

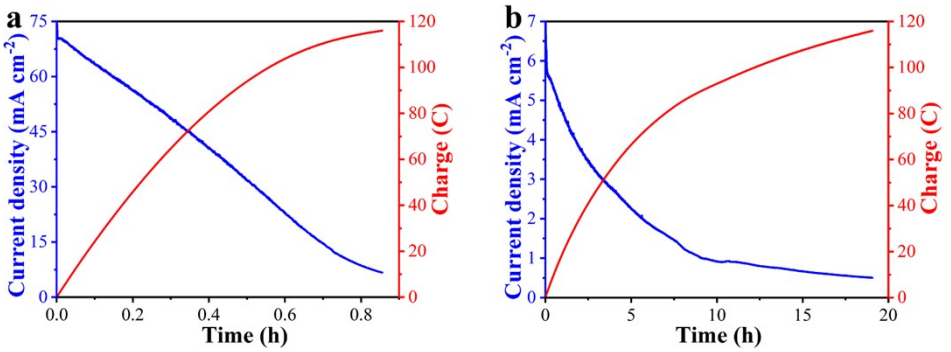

Fig. S12. Corresponding current density change and the accumulated charges during HMF electrolysis catalyzed by (a) RuNPs-$Ni(OH)_2$/NF and (b) $Ni(OH)_2$/NF.

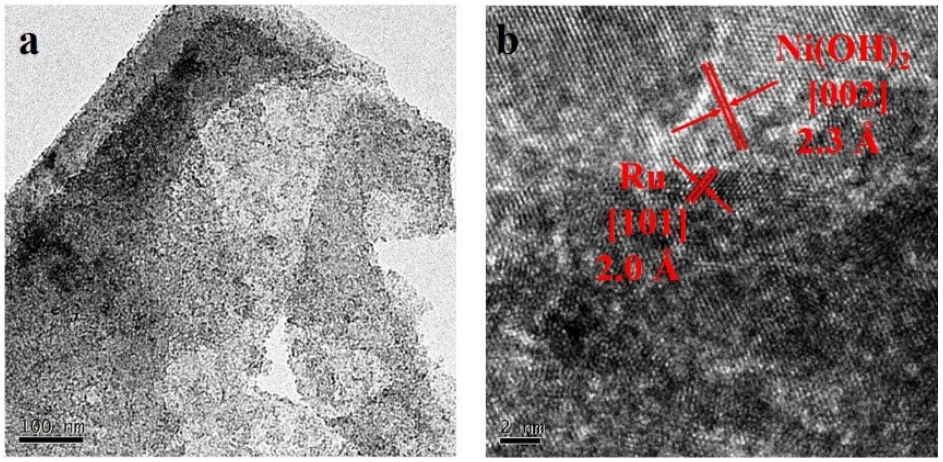

Fig. S13. (a) TEM and (b) HRTEM images of the RuNPs-$Ni(OH)_2$ after HMF electrolysis.

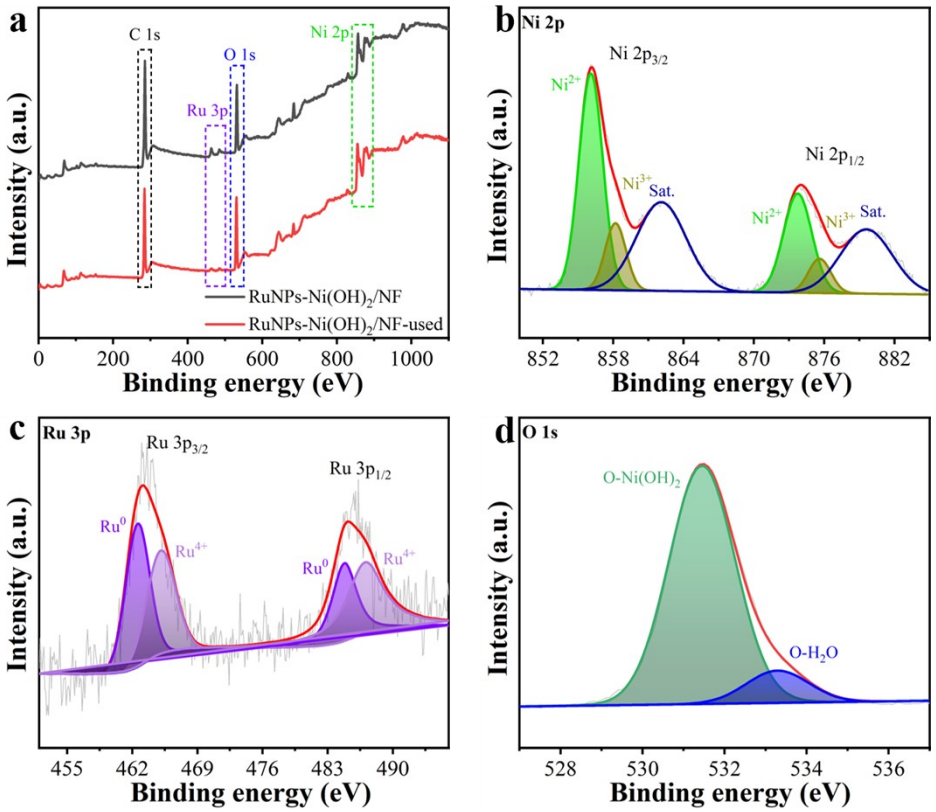

Fig. S14. (a) XPS survey spectrum, (b) Ni 2p peak, (c) Ru 3p peak, and (d) O 1s peak of RuNPs-$Ni(OH)_2$ after HMF electrolysis.

Table S1. HMFOR performance of RuNPs-$Ni(OH)_2$/NF and other reported catalysts.

Electrocatalyst	Electrolyte/HMF concentration	j (mA cm^{-2}) / E (V vs. RHE)	HMF Conversion （%）	FDCA yield (%)	FE (%)	Ref.
RuNPs-$Ni(OH)_2$/NF	1.0 M KOH/10 mM	40/1.35	99.4	99.4	99.2	**This work**
Ni_2P NPA/NF	1.0 M KOH/10 mM	40/1.37	>99	99	99.7	[1]
Ni_3S_2/NF	1.0 M KOH/10 mM	40/1.36	>99	98	98	[2]
MoO_2-FeP@C	1.0 M KOH/10 mM	40/1.37	99.4	98.6	98.7	[3]
Ni_3N@C	1.0 M KOH/10 mM	40/1.37	>99	98	99	[4]
$CuCo_2O_4$	1.0 M KOH/50 mM	40/1.36	98	93.7	94	[5]
NiSe@NiO_x	1.0 M KOH/10 mM	40/1.35	99	98	98	[6]
NiO-Co_3O_4	1.0 M KOH/50 mM	40/1.37	NA	98	96	[7]
Ir-Co_3O_4	1.0 M KOH/50 mM	20/1.49	>99	98	98	[8]
$NiCo_2O_4$@NF	1.0 M KOH/5 mM	10/1.46	99.6	90.8	87.5	[9]
CoFe@NiFe	1.0 M KOH/10 mM	40/1.41	>99	97	-	[10]
Pt/$Ni(OH)_2$	1.0 M KOH/50 mM	40/1.61	>99	98.7	100	[11]
$Ni_{0.5}Co_{2.5}O_4$	1.0 M KOH/50 mM	20/1.45	NA	92.4	90.35	[12]
Ru_1-NiO	1.0 M KOH/50 mM	40/1.62	>99	90	-	[13]
CuO-PdO	1.0 M KOH/50 mM	20/1.41	99.5	96.2	93.7	[14]

References

1. B. You, N. Jiang, X. Liu and Y. Sun, *Angew. Chem. Int. Ed.*, 2016, **55**, 9913-9917.

2. B. You, X. Liu, N. Jiang and Y. Sun, *J. Am. Chem. Soc.*, 2016, **138**, 13639-13646.

3. G. Yang, Y. Jiao, H. Yan, Y. Xie, A. Wu, X. Dong, D. Guo, C. Tian and H. Fu, *Adv. Mater.*, 2020, **32**, 2000455-2000464.

4. N. Zhang, Y. Zou, L. Tao, W. Chen, L. Zhou, Z. Liu, B. Zhou, G. Huang, H. Lin and S. Wang, *Angew. Chem. Int. Ed.*, 2019, **131**, 16042-16050.

5. Y. Lu, C. L. Dong, Y. C. Huang, Y. Zou, Z. Liu, Y. Liu, Y. Li, N. He, J. Shi and S. Wang, *Angew. Chem. Int. Ed.*, 2020, **59**, 19215-19221.

6. L. Gao, Z. Liu, J. Ma, L. Zhong, Z. Song, J. Xu, S. Gan, D. Han and L. Niu, *Appl. Catal. B-Environ.* , 2020, **261**, 118235.

7. Y. Lu, C.-L. Dong, Y.-C. Huang, Y. Zou, Y. Liu, Y. Li, N. Zhang, W. Chen, L. Zhou, H. Lin and S. Wang, *Sci. China Chem.*, 2020, **63**, 980-986.

8. Y. Lu, T. Liu, C. L. Dong, Y. C. Huang, Y. Li, J. Chen, Y. Zou and S. Wang, *Adv. Mater.*, 2021, **33**, 2007056.

9. M. J. Kang, H. Park, J. Jegal, S. Y. Hwang, Y. S. Kang and H. G. Cha, *Appl. Catal. B-Environ.* , 2018, **242**, 85-91.

10. Y. Xie, Z. Zhou, N. Yang and G. Zhao, *Adv. Funct. Mater.*, 2021, **31**, 2102886.

11. B. Zhou, Y. Li, Y. Zou, W. Chen, W. Zhou, M. Song, Y. Wu, Y. Lu, J. Liu, Y. Wang and S. Wang, *Angew. Chem. Int. Ed.*, 2021, **60**, 22908-22914.

12. Y. Lu, T. Liu, Y.-C. Huang, L. Zhou, Y. Li, W. Chen, L. Yang, B. Zhou, Y. Wu, Z. Kong, Z.

Huang, Y. Li, C.-L. Dong, S. Wang and Y. Zou, *ACS Catal.*, 2022, **12**, 4242-4251.

13. R. Ge, Y. Wang, Z. Li, M. Xu, S. M. Xu, H. Zhou, K. Ji, F. Chen, J. Zhou and H. Duan, *Angew. Chem. Int. Ed.*, 2022, **61**, e202200211.

14. P. Zhou, X. Lv, S. Tao, J. Wu, H. Wang, X. Wei, T. Wang, B. Zhou, Y. Lu, T. Frauenheim, X. Fu, S. Wang and Y. Zou, *Adv. Mater.*, 2022, **34**, e2204089.